

Spray pyrolysis synthesis of particles possessing magnetic and fluorescent properties. Application of magnetic/fluorescent particles in immunoassays.

D. Dosev ^a, M. Nichkova ^b, R. Dumas ^c, K. Liu ^c, I. M. Kennedy ^a

^a Department of Mechanical and Aeronautical Engineering, ^b Department of Entomology,
^c Department of Physics, University of California Davis, CA 95616

Abstract

Many types of fluorescent nanoparticles have been synthesized as alternatives to organic dyes in biochemistry. Magnetic beads also have a long history of biological applications. In this work we apply flame spray pyrolysis in order to engineer a novel type of particle that has both fluorescent and magnetic properties. The particles have magnetic cores of iron oxide and a fluorescent shell of europium – doped gadolinium oxide (Eu:Gd₂O₃). Measurements on a Vibrating Sample Magnetometer showed an overall paramagnetic response behavior of the composite particles. Fluorescence spectroscopy showed fluorescent spectra typical for the Eu ion in a Gd₂O₃ host with a narrow emission peak centered near 615 nm. Our synthesis method provides a low-cost, high-rate synthesis that allows a wide range of biological applications of magnetic/fluorescent core/shell particles. We show an immunoassay using the fluorescent properties of the particles.

Introduction

Gas processing of nanostructured materials offers significant advantages over liquid phase chemistry. The process is scalable to high production rates; it can yield material of high purity; a wide range of materials can be formed; and the process can be designed to be both environmentally benign, with no toxic by-products, and energetically efficient. The important characteristics of the product include the particle size distribution, composition and morphology. Rosner et al. (2003; 2002) have recognized the importance of multiple variables in the design and operation of gas phase synthesis processes and have developed an appropriate formalism for treating this problem numerically. Crystal structure may ultimately be predictable with such methods, and in some materials and applications, such as yttrium oxide (yttria), the crystal phase may be an important process variable.

The doping of lanthanides into yttria provides additional functionalities for this material. Lanthanide - doped nanoparticles have attracted a great deal of interest because of their high fluorescent intensity, large Stokes shift and long fluorescence lifetime (Bhargava, 1996; Tissue, 1998). They are used in the display industry (Wakefield et al., 2001) and show promise in sensor applications (Feng et al., 2003). This type of application requires a method for the production of nanopowders (ultra fine particles with diameters below 100 nm) with high production rates (grams per hour range), at low cost, and with the ability to obtain materials with different photoluminescent spectra.

Yttrium oxide (Y_2O_3) is one of the best hosts for lanthanide ions (Hao et al., 2001; Yang et al., 1999) because its ionic radius and crystal structure are very similar to many lanthanide oxides. Doping with a variety of lanthanide ions (Eu for red, Tb for green, Dy for yellow, Tm for blue) (Hao et al., 2001; Vetrone et al., 2004) can yield materials with different fluorescent spectra. The doping concentration of lanthanide ions into Y_2O_3 is of key importance in determining the efficiency of fluorescence emission of these materials (Bazzi et al., 2003; Kang et al., 1999).

We have employed a conventional flame spray pyrolysis technique to produce europium-doped yttrium oxide ($\text{Eu}:\text{Y}_2\text{O}_3$) and $\text{Eu}:\text{Gd}_2\text{O}_3$ nanoparticles with the ultimate purpose to use them as luminescent labels in bioassays. Our immediate goal is to examine the impact of nanoparticle size on crystal phase, and to demonstrate the feasibility of using spectroscopy as a diagnostic for the synthesis of materials such as yttria and lanthanide-doped yttria. We have also synthesized Fe_2O_3 nanoparticles that are paramagnetic. These particles are used as the core in a $\text{Eu}:\text{Gd}_2\text{O}_3$ luminescent shell.

Experimental

Nanoparticle Synthesis. A schematic diagram of the burner used in this study is shown in Fig. 1. The burner consists of a nebulizer and a co-flow jacket. The nebulizer has an inner nozzle made of 20 gage SS304 capillary tube (0.81 mm OD) and an outer jacket. The inner nozzle extends through a hole in the outer jacket approximately 1 mm in diameter and ends flush with the top of the outer jacket. A narrow annular gap is formed between the inner nozzle and the outer jacket. An ethanol solution containing 2.5 mM $\text{Eu}(\text{NO}_3)_3$ and 50 mM $\text{Y}(\text{NO}_3)_3$ was pumped by a syringe pump (Cole-Parmer) at 40 mL/h into the inner nozzle of the nebulizer. Air, at 2 L/min, flowed through the annular gap surrounding the inner nozzle at high speed to atomize the ethanol solution containing the precursor materials. The solution was atomized to form a spray above the tip of the nebulizer. The co-flow jacket supplied H_2 at 2 L/min and co-flow air at 10 L/min, to form a hydrogen-air diffusion flame surrounding the outlet of the nebulizer. The flame temperature in the H_2 flame was measured with a coated thermocouple to be about 2100 °C. The H_2 diffusion flame served as a pilot for the spray flame that was formed by the combustible ethanol droplets containing the europium and yttrium precursors. Reactions took place within the flame to form $\text{Eu}:\text{Y}_2\text{O}_3$ nanoparticles. A cold finger was used for collecting the $\text{Eu}:\text{Y}_2\text{O}_3$ particles thermophoretically above the flame. The production rate of this synthesis procedure was about 400 – 500 mg/h.

Figure 2 shows the spray droplet size distribution, which was measured using a standard laser diffraction system (Model 2600, Malvern Instruments, UK). The droplet sizes were measured without ignition of the flame. Droplet diameters between 1 and 100 μm were found. This wide droplet size distribution leads to a correspondingly wide particle size distribution in the nanoparticle powder that is formed.

Nanoparticle Separation

The as-synthesized particles were suspended in methanol in an ultrasonic bath for 30 min in order to break any weak agglomerates formed during the collection process. The primary $\text{Eu}:\text{Y}_2\text{O}_3$ particles had a relatively wide size distribution from 5 to 300 nm as determined by TEM. Two portions with narrower size distributions were extracted using size selective centrifugation with a Sorvall® RC5B Plus Centrifuge (Kendro Laboratory Products). First, the nanoparticles-methanol suspension was centrifuged at 1000g for 16 min. In this step, all the

nanoparticles with diameters bigger than about 50 nm were settled. The supernatant containing nanoparticles with diameters smaller than 50 nm was collected and the methanol was evaporated.

Nanoparticle Characterization

The size distributions of the two separated nanoparticle suspensions are shown in Fig. 3. They were determined using a Philips CM-12 Transmission Electron Microscope (TEM). More than 100 individual particle sizes were measured for each sample. The smaller particle portion contained particles with diameters from 5 nm to 60 nm. The larger particle portion contained particles with diameters from about 50 nm to 200 nm. There was a small size overlap between the two samples at about 50 nm as one can see from Fig. 3. This is expected with the centrifugal separation method.

Representative TEM images for the two fractions are shown in Fig. 4. The collected particles were non-aggregated, a requirement for sensor applications. Both small and big particles exhibited a fully dense morphology. Many of the smaller particles (Fig. 4A) appeared to be faceted. On the other hand, the larger particles (Fig. 4B) had an overall spherical shape but in some cases, as seen in this example, smaller inclusions of the type seen in Fig. 4A were apparent in the center of the larger sphere. Close examination of images such as Fig. 4B suggested that the larger particles were polycrystalline with multiple domains apparent in the material surrounding the core.

Optical characterization of the Eu:Y₂O₃ nanoparticles was carried out by using laser – induced fluorescence. Colloidal suspensions of 1 mg ml⁻¹ in methanol were prepared from each of the two sized fractions. The nanoparticles were excited non-selectively with a pulsed laser beam of approximately 100 μJ at 260 nm wavelength, using an Opolette™ tunable pulsed optical parametric oscillator (OPO) laser (Opotek, CA); we found that it was not possible to obtain useful spectra with site-selective excitation of the particles in the visible region of the spectrum due to the small concentration of particles and the relatively small absorption cross-sections at the visible wavelengths that correspond to crystal sites. The fluorescence spectra were recorded using a Spectra Pro 300i gated intensified spectrometer (Princeton Instruments Inc).

Application to bioassays

Coating of Eu:Gd₂O₃ nanoparticles with avidin.

Eu:Gd₂O₃ nanoparticles (1 mg) were suspended using an ultrasonic bath in 1 ml of 25 mM carbonate-bicarbonate buffer, pH 8.6, in a polypropylene tube, previously coated with 0.5% BSA to avoid loss of avidin to the tube walls. A solution of 2 mg ml⁻¹ avidin (100 μl) was added to the particle suspension and incubated in a rotating mill overnight at room temperature. The suspension was then centrifuged at 15000×g for 3 minutes. The supernatant was discarded and the nanoparticle pellet was resuspended in the same buffer to wash off the excess protein. This washing procedure was repeated 3 times. In order to ensure that no bare particle surface remained, the avidin - Eu:Gd₂O₃ nanoparticles were incubated in 1 ml of 0.5 mg ml⁻¹ BSA solution in 25 mM phosphate buffer for 1 h at room temperature in the rotating mill. After three consecutive washings by centrifugation and resuspension, the avidin - Eu:Gd₂O₃ nanoparticles were used for the micropattern detection assays.

The surface saturation capacity of the nanoparticles with respect to avidin was evaluated following the same coating procedure, using avidin-rhodamine complex instead of avidin. After efficient washing of the excess avidin-rhodamine from the coating solution, the nanoparticle

pellet was resuspended in 100 μ l of carbonate-bicarbonate buffer. The fluorescence of rhodamine (excitation 520 nm, emission 550 nm) adsorbed on the particle surface was measured on the microplate reader and was used as an indication for the amount of adsorbed avidin molecules.

An identical coating with neutravidin rather than with avidin produced a smaller amount of protein adsorbed to the nanoparticle's surface. This result strongly suggests that the higher positive charge of hen egg avidin (PI = 10.0), compared to that of neutravidin (PI = 6.3), contributes to the stronger adsorption to the negatively charged particle surface. This observation is consistent with other studies on protein adsorption onto quantum dots based on electrostatic interactions.

Microcontact printing of biotinylated BSA: Substrate, stamp and sample preparation.

A silicon (100) wafer was used as a solid substrate for microcontact printing of proteins and the consecutive specific interactions. Prior to use, the silicon wafer was thoroughly washed in ultrasound bath in acetone, ethanol and deionized water for 10 min each. Finally, it was dried under a nitrogen stream. The PDMS stamp was washed by sonication in ethanol (3x10 min), dried under nitrogen and exposed to the solution of the inking protein (50 μ g ml⁻¹ BSA-b in PBS) for 40 min. Excess solution was removed and the stamp was dried under a stream of nitrogen gas. After inking, the stamp was brought into contact with the silicon wafer substrate; a very small amount of force was applied to make a good contact between both surfaces. The stamp was removed after 2 min, and the wafer was rinsed with PBS and deionized water and dried under nitrogen. The stamp could be used about 50 times without degradation of the printing capability when rinsed with water, water:ethanol mixture (80:20) and cleaned by sonication in ethanol (3x10 min) after each inking and printing cycle.

After micro contact printing of the BSA-b, the uncovered areas on the silicon substrate were blocked by immersing the wafer into a 2 mg ml⁻¹ BSA solution in PBS for 1 h in order to avoid further non-specific binding and/or sticking. After washing and drying, the wafer was incubated with a suspension of the avidin coated Eu:Gd₂O₃ nanoparticles in carbonate-bicarbonate buffer) for 1 h in a shaker to allow for specific interaction between the avidin and biotin. After the interaction took place, the substrate was rinsed with buffer and water, and dried under nitrogen before fluorescence and AFM studies.

Luminescence microscopy imaging.

Luminescence images were acquired with a fluorescence microscope equipped with a computer - controlled CCD camera. A 100 W Hg lamp was used to excite the luminescence of the Eu:Gd₂O₃ nanoparticles. A dichroic cube with a threshold wavelength of 400 nm was used to separate the UV excitation ($\lambda_{\text{ex}} < 400$ nm) from the visible luminescent emission ($\lambda_{\text{em}} > 400$ nm). The CCD camera, image capture and analysis were controlled by "Spot" software.

Atom force microscopy characterization

All the AFM images were obtained using the contact mode at a scan speed of 1-2 Hz. The image force was under 5 nN. The topography and lateral force images were taken in air at room temperature.

Coating of the nanoparticles with avidin

Because the avidin-biotin interaction has a high binding constant, this assay is widely used in molecular biology, immunoassay, diagnostics, and biosensor research. A demonstration using the avidin and biotin reaction system is the logical first step in an evaluation of a new format for biosensors, protein chips, and other miniaturized analytical devices. Thus, we have chosen the avidin-biotin system as a model system in our studies in order to demonstrate the effectiveness of Eu:Gd₂O₃ nanoparticles as luminescent labels for micropattern imaging.

Avidin has been found to adsorb tightly to a variety of surfaces, such as dye-doped silica nanoparticles, carbon nanotubes and quantum dots due to electrostatic and/or hydrophobic interactions. Here, we take advantage of the negatively charged surface of the Eu:Gd₂O₃ nanoparticles to coat them with the avidin molecules using electrostatic interactions. The coating was carried out according to the experimental procedure described above. There are several advantages offered by this coating method: it is a one-step procedure (thereby avoiding chemical functionalization and conjugation steps); proteins retain their activity; conjugates are stable in a variety of buffers; the number of binding sites on the surface can be controlled by varying the coating concentration and they can be quantified easily; the nanoparticle's luminescence is not affected by the protein layer; the nanoparticle surface can be efficiently blocked to avoid non-specific binding in immunoassays.

For evaluation of the avidin coating, Eu:Gd₂O₃ particles were coated with rhodamine-labeled avidin, following the procedure described in the experimental section. Using the measured fluorescence intensity of rhodamine, the amount of avidin that was adsorbed on the particle's surface was evaluated for different coating concentrations of avidin-Rhodamine per 1 mg nanoparticles (Fig. 5). For concentrations up to 200 µg ml⁻¹, the amount of adsorbed avidin increased proportionally to the coating concentration, showing that the amounts of avidin were not enough to form dense monolayers on the particles surfaces. For concentrations higher than 200 µg ml⁻¹, the adsorption of avidin did not depend on the coating concentration, indicating saturation of the particles' surfaces with avidin, suggesting the formation of a monolayer.

Fluorescence imaging of BSA-Biotin micropatterns with avidin - Eu:Gd₂O₃ nanoparticles

The preparation of the BSA-Biotin micropatterns and their interaction with the avidin coated Eu:Gd₂O₃ nanoparticles is schematically presented in Fig. 6. The corresponding luminescent image is shown in Fig. 7. A series of alternating bright strips and dark strips can be observed. The actual width of the strips is 5 µm, which corresponds to the features of the PDMS stamp used for BSA-b printing. The bright strips correspond to the luminescent Eu:Gd₂O₃ – avidin complexes that were specifically bound to the printed BSA-b. The dark strips, on the other hand, correspond to the blocked space between the printed strips where no avidin-coated particles were present. Although not all the bright strips had perfectly uniform fluorescent intensity, they were covered with specifically bound luminescent particles without large gaps. Densely packed bound particles showed up as higher intensity spots while areas with lower surface density of bound particles were dimmer. On the other hand, very few particles could be observed in the BSA – passivated areas, demonstrating very low nonspecific binding in this case. The presence of clearly distinguishable fluorescent strips showed that the specific binding of avidin to biotin was not disturbed by the particles. In addition, the absence of particles between the strips confirmed that the blocking of the silicon substrate and the nanoparticles with BSA was sufficient to prevent non-specific binding of nanoparticles onto the substrate.

Another important conclusion is that the non – uniform size distribution of the nanoparticles may not disturb this type of application. This makes possible the use of polydispersed particles instead of expensive monodispersed particles. The lack of photobleaching of the Eu:Gd₂O₃ nanoparticles allowed the fluorescent image to be observed for an unlimited period of time facilitating image optimization.

AFM characterization of BSA-Biotin micropatterns with avidin - Eu:Gd₂O₃ nanoparticles

We have employed AFM to image the immobilized avidin-Eu:Gd₂O₃ on a single particle level. The presence of solid nanoparticle labels with sizes larger than those of proteins on the substrate surface made it possible to evaluate the density of specifically and non-specifically bound particles. The surface density of specifically bound particles on the strips was much higher than the density of non-specifically bound particles shown as scattered bright spots between the line patterns. The selectivity achieved here is the basis for applying this approach as a detection technique.

The non-specific binding of particles could be minimized possibly by further optimization of the coating and washing processes. We believe that the non-uniform density of the specifically bound particles could be partially due to reduced diffusion near the substrate surface and partially due to formation of small aggregates of particles during the incubation. This effect could be avoided by optimization of the incubation protocols. According to the cursor profile, the particles on the strips have heights between about 10 and 250 nm. The majority of the particles exhibit heights between 50 and 100 nm. This height measurement is consistent with the particle size known from TEM studies. It is clear that these particles are the immobilized avidin-coated nanoparticles. Spatial resolution and the uniformity of protein micropattern visualization could be improved by using smaller, more nearly monodispersed particles.

References

- Arabi-Katbi, O. I., Pratsinis, S. E., Morrison, P. W., and Megaridis, C. M. (2001) Monitoring the flame synthesis of TiO₂ particles by in-situ FTIR spectroscopy and thermophoretic sampling. *Combust. Flame*, **124**, 560.
- Bazzi, R., Flores-Gonzalez, M. A., Louis, C., Lebbou, K., Dujardin, C., Brenier, A., Zhang, W., Tillement, O., Bernstein, E., and Perriat, P. (2003) Synthesis and luminescent properties of sub-5-nm lanthanide oxides nanoparticles. *J. Luminesc.*, **102-103**, 445.
- Bhargava, R. N. (1996) Doped nanocrystalline materials -- Physics and applications. *J. Luminesc.*, **70**, 85.
- Bihari, B., Eilers, H., and Tissue, B. M. (1997) Spectra and dynamics of monoclinic Eu₂O₃ and Eu³⁺: Y₂O₃ nanocrystals. *J. Luminesc.*, **75**, 1.
- Chalek, C. L., and Gole, J. L. (1976) Chemiluminescence spectra of Sc and YO: observation and analysis of the A¹₂Δ - X²₁Σ⁺ band system. *J. Chem. Phys.*, **65**, 2845.
- Chen, G., Stump, N. A., Haire, R. G., and Peterson, J. R. (1992) Study of the phase behavior of Eu₂O₃ under pressure via luminescence of Eu³⁺. *J. Alloys Comp.*, **181**, 503.

- Ehrman, S. H. (1998) Effect of internal pressure on nanoparticle coalescence. *J. Aerosol Sci.*, **29**, S31.
- Ehrman, S. H., Friedlander, S. K., and Zachariah, M. R. (1998) Characteristics of SiO₂/TiO₂ nanocomposite particles formed in a premixed flat flame. *J. Aerosol Sci.*, **29**, 687.
- Eilers, H., and Tissue, B. M. (1996) Laser spectroscopy of nanocrystalline Eu₂O₃ and Eu³⁺:Y₂O₃. *Chem. Phys. Lett.*, **251**, 74.
- Feng, J., Shan, G. M., Maquieira, A., Koivunen, M. E., Guo, B., Hammock, B. D., and Kennedy, I. M. (2003) Functionalized europium oxide nanoparticles used as a fluorescent label in an immunoassay for atrazine. *Anal. Chem.*, **75**, 5282.
- Gribb, A. A., and Banfield, J. F. (1997) Particle size effects on transformation kinetics and phase stability in nanocrystalline TiO₂. *Am. Mineral.*, **82**, 717.
- Hao, J., Studenikin, S. A., and Cocivera, M. (2001) Blue, green and red cathodoluminescence of Y₂O₃ phosphor films prepared by spray pyrolysis. *J. Luminesc.*, **93**, 313.
- Hoekstra, H. R., and Gingerich, K. A. (1964) High-Pressure B-Type Polymorphs of Some Rare-Earth Sesquioxides. *Science*, **146**, 1163.
- Husson, E., Proust, C., Gillet, P., and Itie, J. P. (1999) Phase Transitions In Yttrium Oxide At High Pressure Studied By Raman Spectroscopy. *Mat. Res. Bull.*, **34**, 2085–2092.
- Jones, S. L., Kumar, D., Singh, R. K., and Holloway, P. H. (1997) Luminescence of pulsed laser deposited Eu doped yttrium oxide films. *Appl. Phys. Lett.*, **71**, 404.
- Kang, Y. C., Park, S. B., Lenggoro, I. W., and Okuyama, K. (1999) Gd₂O₃:Eu phosphor particles with sphericity, submicron size and non-aggregation characteristics. *J. Phys. Chem. Solids*, **60**, 379.
- Kang, Y. C., Roh, H. S., and Park, S. B. (2000) Preparation of Y₂O₃:Eu phosphor particles of filled morphology at high precursor concentrations by spray pyrolysis. *Adv. Mat.*, **12**, 451.
- Kang, Y. C., Roh, H. S., Park, S. B., and Park, H. D. (2002) High luminescence Y₂O₃: Eu phosphor particles prepared by modified spray pyrolysis. *J. Mat. Sci. Lett.*, **21**, 1027.
- Katagiri, S., Ishizawa, N., and Marumo, F. (1993) A new high temperature modification of face-centered cubic Y₂O₃. *Powder Diff.*, **8**, 60.
- Kim, C. S., Nakaso, K., Xia, B., and Okuyama, K. (2005) A New Observation on the Phase Transformation of TiO₂ Nanoparticles Produced by a CVD Method. *Aerosol Science and Technology*, **39**, 104.
- Rosner, D. E., McGraw, R., and Tandon, P. (2003) Multivariate population balances via moment and Monte Carlo simulation methods: An important sol reaction engineering bivariate example and "mixed" moments for the estimation of deposition, scavenging, and optical properties for populations of nonspherical suspended particles. *Ind. Engr. Chem. Res.*, **42**, 2699.
- Rosner, D. E., and Pyykonen, J. J. (2002) Bivariate moment simulation of coagulating and sintering nanoparticles in flames. *AIChE J.*, **48**, 476.
- Shikao, S., and Jiye, W. (2001) Combustion synthesis of Eu³⁺ activated Y₃Al₅O₁₂ phosphor nanoparticles. *J. Alloys Comp.*, **327**, 82.

- Skandan, G., Foster, C. M., Frase, H., Ali, M. N., Parker, J. C., and Hahn, H. (1992) Phase characterization and stabilization due to grain size effects of nanostructured Y_2O_3 . *Nano. Mat.*, **1**, 313.
- Tissue, B. M. (1998) Synthesis and luminescence of lanthanide ions in nanoscale insulating hosts. *Chem. Mat.*, **10**, 2837.
- Tissue, B. M., and Yuan, H. B. (2003) Structure, particle size, and annealing of gas phase-condensed $Eu^{3+}:Y_2O_3$ nanophosphors. *J. Solid State Chem.*, **171**, 12.
- Vander Wal, R. L., Berger, G. M., Ticich, T. M., and Patel, P. D. (2002) Application of laser-induced incandescence to the detection of carbon nanotubes and carbon nanofibers. *Appl. Optics*, **41**, 5678.
- Vander Wal, R. L., Ticich, T. M., West, J. R., and Householder, P. A. (1999) Trace metal detection by laser-induced breakdown spectroscopy. *Appl. Spec.*, **53**, 1226.
- Vetrone, F., Boyer, J. C., Capobianco, J. A., Speghini, A., and Bettinelli, M. (2004) A spectroscopic investigation of trivalent lanthanide doped Y_2O_3 nanocrystals. *Nanotech.*, **15**, 75.
- Wakefield, G., Holland, E., Dobson, P. J., and Hutchison, J. L. (2001) Luminescence properties of nanocrystalline $Y_2O_3:Eu$. *Adv. Mat.*, **13**, 1557.
- Wijchers, T., Dijkerman, H. A., Zeegers, P. J. T., and Alkemade, C. T. J. (1980) Fluorescence spectra of laser-excited YO molecules in a H_2-O_2-Ar flame. *Spec. Acta*, **35B**, 271.
- Williams, D. K., Yuan, H., and Tissue, B. M. (1999) Size dependence of the luminescence spectra and dynamics of $Eu^{3+}:Y_2O_3$ nanocrystals. *J. Luminesc.*, **83-84**, 297.
- Xing, Y., Rosner, D. E., Koylu, U. O., and Tandon, P. (1997) Morphological evolution of nanoparticles in diffusion flames: Measurements and modeling. *AIChE J.*, **43**, 2641.
- Xing, Y. C., Koylu, U. O., and Rosner, D. E. (1996) Synthesis and restructuring of inorganic nano-particles in counterflow diffusion flames. *Combust. Flame*, **107**, 85.
- Xing, Y. C., Koylu, U. O., and Rosner, D. E. (1999) In situ light-scattering measurements of morphologically evolving flame-synthesized oxide nanoaggregates. *Appl. Optics*, **38**, 2686.
- Yang, H.-S., Hong, K. S., Feofilov, S. P., Tissue, B. M., Meltzer, R. S., and Dennis, W. M. (1999) Electron-phonon interaction in rare earth doped nanocrystals. *J. Luminesc.*, **83-84**, 139.
- Zhang, H. Z., and Banfield, J. F. (1998) Thermodynamic analysis of phase stability of nanocrystalline titania. *J. Mat. Chem.*, **8**, 2073.

Figure Captions

Figure 1. Schematic description of the burner used for synthesis of the nanoparticles.

Figure 2. Size distribution of the spray droplets injected in the flame

Figure 3. Size distributions of the two nanoparticle fractions, separated by centrifugation. A) Small particles; B) Big particles

Figure 4. Representative bright field TEM images of nanoparticles separated by centrifugation. A - small particle fraction, B - large particle fraction

Figure 5 Coating of nanoparticles

Figure 6 Schematic of assay

Figure 7 Luminescent image of microprinted strips with bound nanoparticles

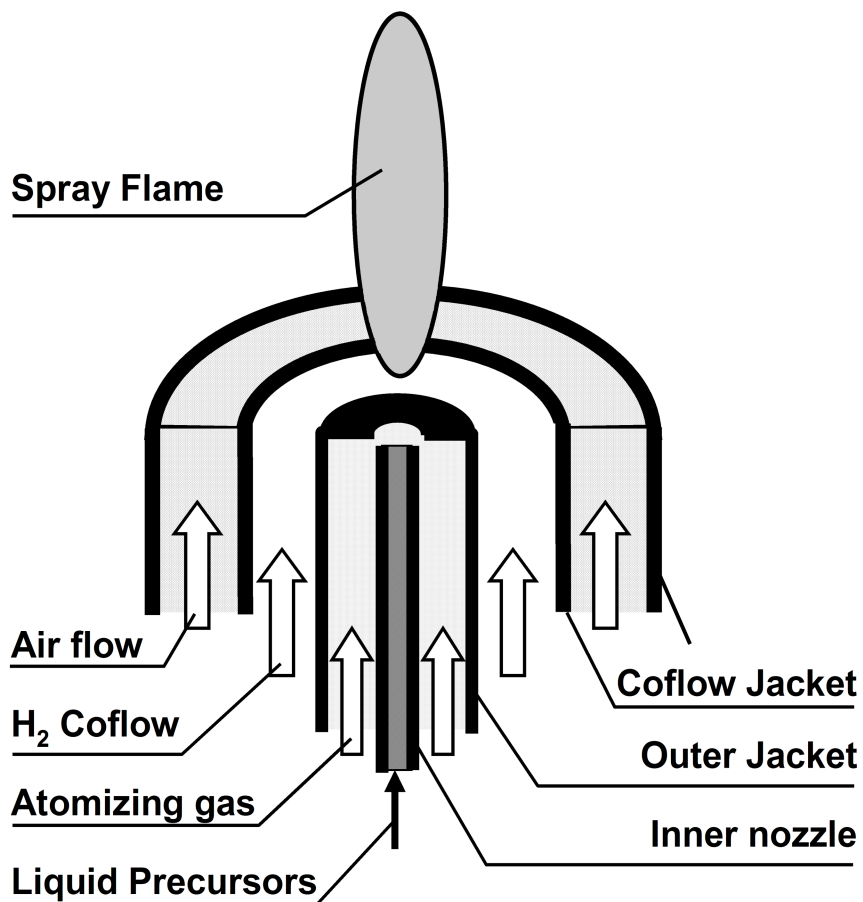


Figure 1

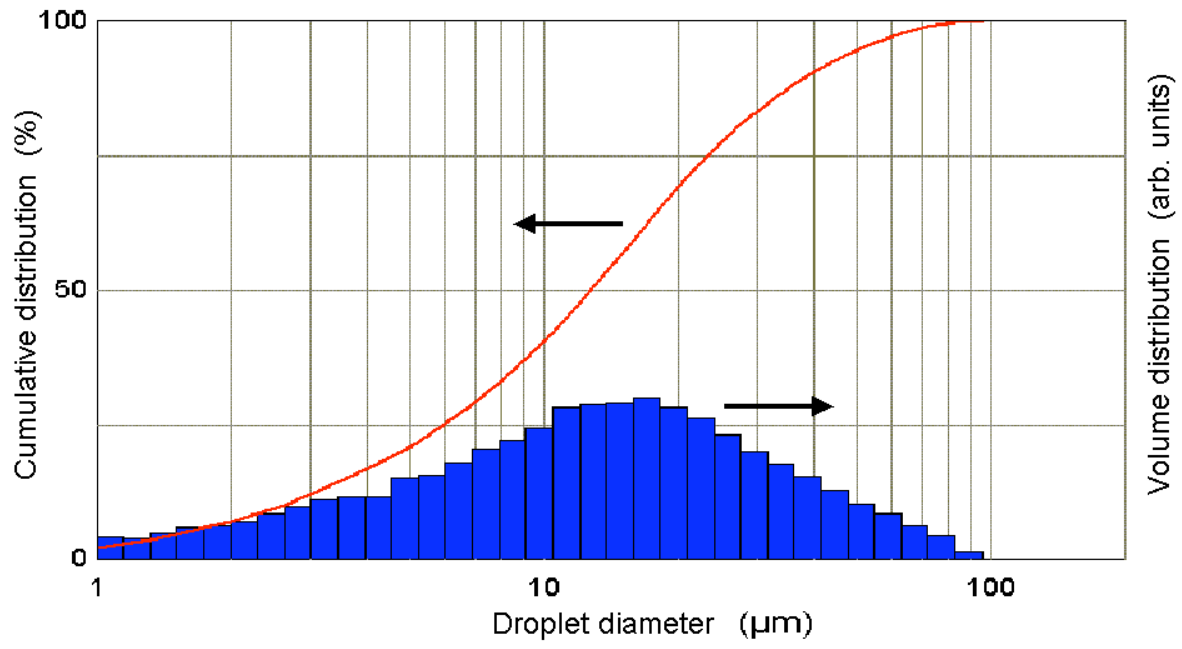


Figure 2

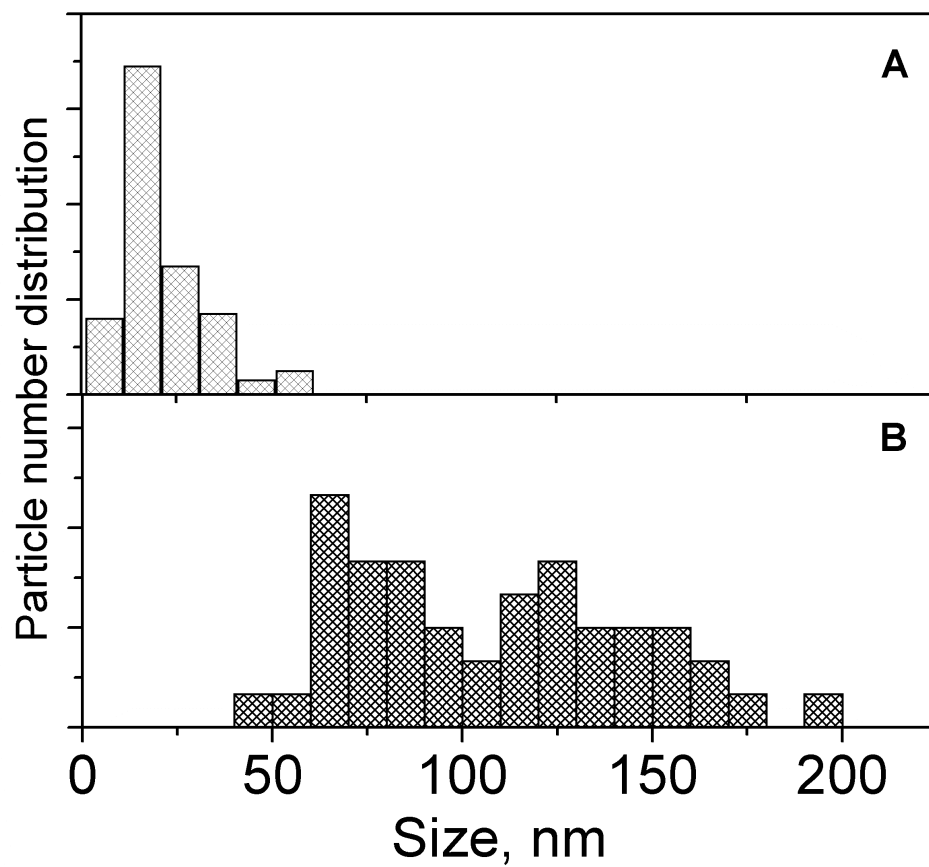
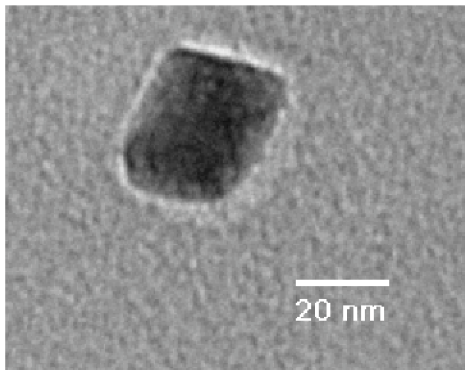
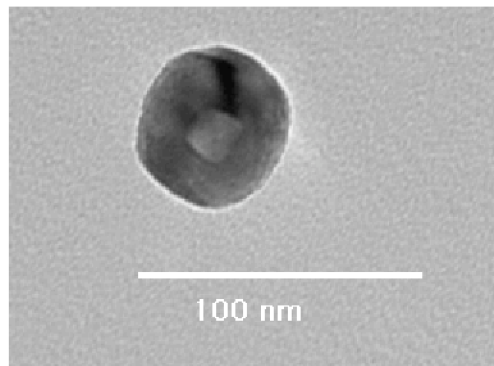


Figure 3



A



B

Figure 4

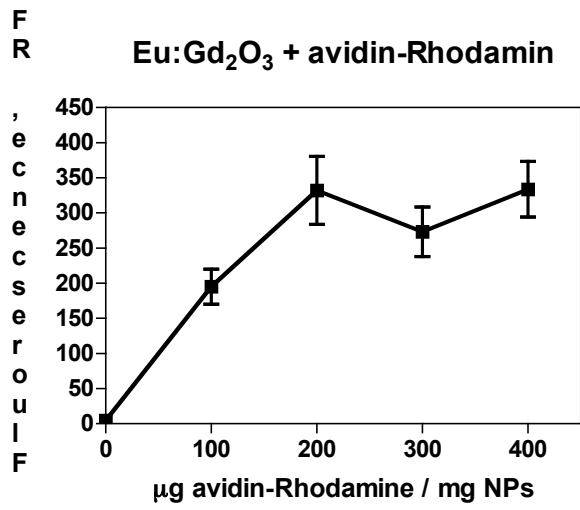


Figure 5

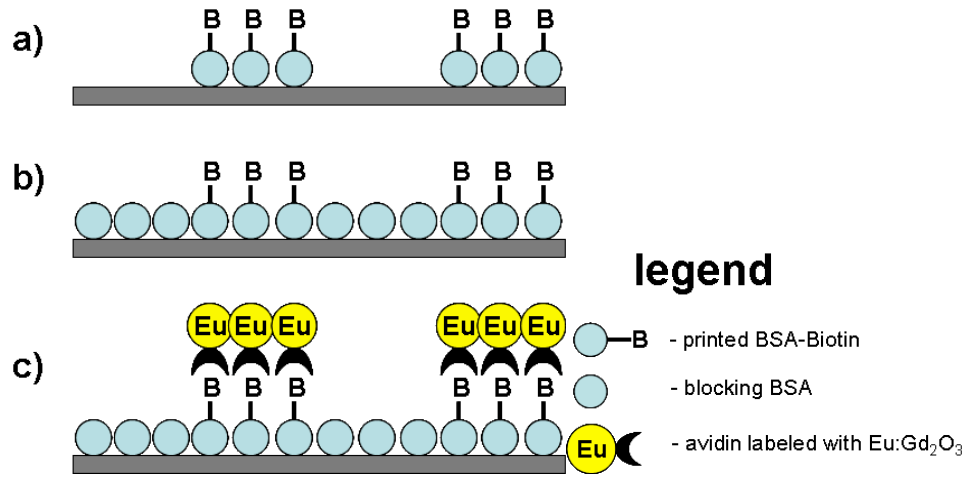


Figure 6

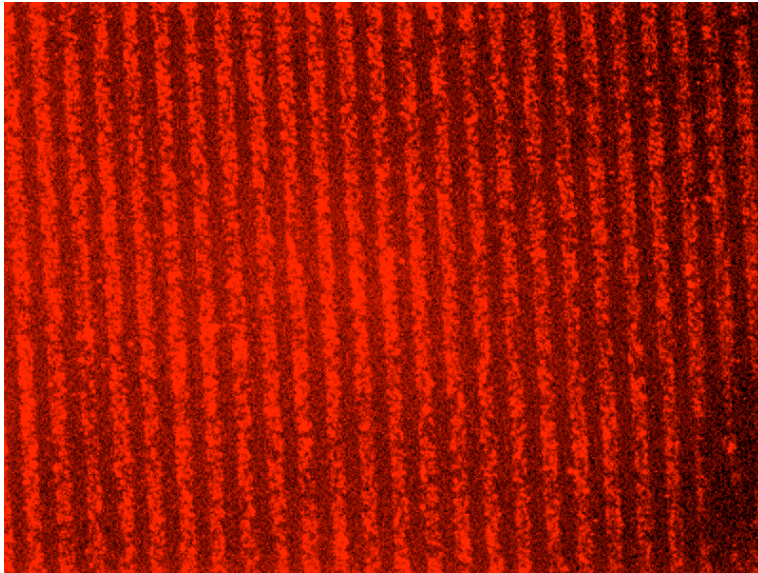


Figure 7